Chemical Science

EDGE ARTICLE

Check for updates

All publication charges for this article have been paid for by the Royal Society of Chemistry

Solvent-induced orientation of FAPbI₃ single crystals for highly efficient self-powered X-ray detectors

Fang Liu,[a] Yu Zou, [b] Pengxiang Wang,[c] Hu Wang, [c] Jiahao Guo,[a] Yugang Liang,[a] Haifei Wang,[a] Wenji Zhan,[a] Zhengzheng Dang, [b] Jixin Wu,[b] Yanming Wang, [b] Bowei Li,[b] Yanfeng Miao,[ad] Yuetian Chen, [ad] Yao Wang*[bd] and Yixin Zhao [*abde]

Perovskites are promising materials for use in self-powered X-ray detectors. However, the presence of defects causes unsatisfactory sensitivity in the prepared devices. Tuning crystal orientation has been confirmed to be an effective means of reducing the defects of perovskites. Here, we report the co-development of (100), (110) and (111) crystal orientations in FAPbI₃ SCs for the first time by inducing the target facets to be the lowest surface energy facets within the selected solvents. The size of the formed facets is large enough to evaluate their properties without interference from non-dominant facets. Compared to (110)- and (111)-oriented FAPbI₃ SCs, the (100)-oriented one manifests reduced trap-state density and suppression of ionic migration. It thus promotes charge collection, demonstrating superior response performance under both visible-light and X-ray illuminations. Moreover, such orientation engineering enables FAPbI₃ SCs to be excellent candidates for self-powered X-ray detectors. High sensitivity close to 5000 μC Gy$_{air}^{-1}$ cm^{-2} was achieved when using 30 keV of X-ray energy, which is the record value among all the self-powered X-ray detectors constructed exclusively by perovskites, even surpassing the devices assisted by heterojunctions. Hence, our findings confirm that solvent-induced orientation engineering has great potential to enable perovskite SCs to be the superior choice for self-powered X-ray photodetectors with high performance.

Introduction

Self-powered X-ray detectors have attracted widespread attention in many fields, because they can avoid heavy external bias power supply systems and reduce corresponding noise interference to potentially realize better portability and higher resolution.[1–3] The critical point for preparing self-powered X-ray detectors with high performance is to increase the free charge lifetime and carrier mobility within the devices. Achieving these objectives requires suppressing deep-level traps, as they exert adverse effects on photocurrent gain, whereas shallow traps can effectively induce such gain.[4,5] Due to the excellent defect

tolerance brought about by the characteristics of soft lattice ionic semiconductors, metal halide perovskites (MHPs) reveal high optical absorption coefficients, large free charge lifetimes and bipolar characteristics.[6–8] Under illumination, ionic redistribution of the MHPs can induce the generation of built-in electric fields in the absence of an applied external bias.[9–11] This thus suggests that MHPs can be ideal candidates for self-powered X-ray detectors. However, most of the already existing self-powered perovskite X-ray detectors require the introduction of extra charge transport materials (*e.g.*, TiO₂ or C₆₀ for electron transport layers (ETLs), and PTAA or NiO$_x$ for hole transport layers (HTLs))[4,5,12] or the construction of heterojunctions to increase the carrier mobility-lifetime (μτ) product.[3,13–15] This appears to have failed to fully leverage the inherent characteristic advantages of perovskites. In addition, two-dimensional or quasi two-dimensional perovskites may demonstrate lower noise for the prepared X-ray detectors because of the larger ion migration activation energy, but the existence of disorder energy landscapes causes worse free charge transport properties than three-dimensional perovskites, thus resulting in a disadvantage in building high-performance detectors.[16,17]

Tuning crystal orientation holds significant promise for substantially enhancing the intrinsic properties of MHPs, such

aSchool of Environmental Science and Engineering, Frontiers Science Center for Transformative Molecules, Shanghai Jiao Tong University, Shanghai 200240, China. E-mail: yixin.zhao@sjtu.edu.cn

bFuture Photovoltaics Research Center, Global Institute of Future Technology (GIFT), Shanghai Jiao Tong University, Shanghai 200240, China. E-mail: yao.wang1993@sjtu.edu.cn

cLaboratory of Thin Film Optics, Shanghai Institute of Optics and Fine Mechanics, Chinese Academy of Sciences, Shanghai 201800, China

dShanghai Non-carbon Energy Conversion and Utilization Institute, Shanghai 200240, China

eState Key Laboratory of Green Papermaking and Resource Recycling, Shanghai Jiao Tong University, Shanghai 200240, China

as suppressing trap states and ion migration,[18–21] because the facets with different orientations feature distinct atomic arrangements and coordination environments, leading to different crystal nucleation and growth processes.[22,23] Previous studies have suggested that it is feasible to manipulate the crystal orientation through the implementation of diverse strategies, with the ultimate goal of achieving the desired application.[20,22–27] Hence, controlling the orientation may fully leverage the intrinsic property advantages of MHPs in photodetectors, especially for self-powered X-ray detectors.

FAPbI$_3$ presents great potential in the application of self-powered X-ray detectors, because it reveals higher decomposition temperature and mobility-lifetime product than MAPbI$_3$, as well as better room-temperature stability of the photoactive phase than CsPbI$_3$.[4,7,28,29] Remarkably,the facet tuning of FAPbI$_3$ perovskite has been realized by introducing appropriate additives to reduce the surface energy of the corresponding dominant orientation.[24,26,30] However, for these studies based on polycrystalline films, the single orientation is difficult to be accurately assessed due to the inevitable interference from other orientations. In comparison, FAPbI$_3$ single crystals (SCs) have the potential to expose large enough single-crystal facets to perform accurate detections under the current technological conditions. In this study, we successfully achieved co-development of (100), (110), and (111) crystal orientations in FAPbI$_3$ SCs for the first time by inducing the target facets to be the lowest surface energy in the screened solvents. This enables us to accurately evaluate the characteristic differences on these three facets without interference from other exposed orientations. We found that FAPbI$_3$ SCs with (100) orientation exhibit lower trap density and less ion migration than those with (110) and (111) orientations, contributing to a larger μτ product. In the present study, (100)-oriented FAPbI$_3$ single crystals enable transport-layer-free devices to achieve record-high sensitivity and ultralow detection limits under low-energy X-ray irradiation and zero-bias operation. This promotes us to realize superior self-powered perovskite SC X-ray detectors. A sensitivity value close to 5000 μC Gy$_{air}^{-1}$ cm^{-2} was achieved for the self-powered X-ray detectors based on (100) oriented FAPbI$_3$ SCs. It is the record value among all the self-powered perovskite X-ray detectors ever reported, which are not assisted by extra charge transport materials.

Results and discussion

Solvent-induced orientation of FAPbI$_3$ SCs

To evaluate the FAPbI$_3$ SCs, the inverse temperature solubility method was employed to synthesize the samples with different orientations by applying specific solvents (Fig. S1).[31–33] The photographs of the obtained FAPbI$_3$ SCs were inserted in Fig. 1a. The bandgaps of these SCs are ~1.47 eV as evaluated by the Tauc plots of absorbance with photon energy (Fig. S2). X-ray diffraction (XRD) patterns reveal that γ-valerolactone (GVL) induced the prepared SCs to exhibit diffraction angles at 13.9°, 28.0°, and 42.6°, which correspond to (100), (200), and (300) crystal facets, respectively (Fig. 1a). By comparison, the SCs based on γ-butyrolactone (GBL) exhibited different diffraction

angles from those based on GVL, which are at 19.8° and 40.2°, corresponding to (110) and (220) crystal facets, respectively. Moreover, the diffraction angles at 24.5° and 49.8° observed for 2-methoxyethanol (2-ME) based SCs are also different from those based on GVL and GBL, which represent (111) and (222) crystal facets, respectively. These results demonstrate that the prepared FAPbI$_3$ SCs resulting from GVL, GBL and 2-ME tend to form (100), (110) and (111) orientations, respectively. The increasingly shrinking lattice constants (Fig. S3) from the (111) crystal facet to the (110) crystal facet and then to the (100) crystal facet were caused by the increasingly short Pb–I bonds, which is evidenced by the measured increasing binding energies of Pb 3f (Fig. 1b) and I 3d (Fig. S4) in X-ray photoelectron spectroscopy (XPS).[7] This thus causes the Pb–I octahedral frameworks of (100)-based SCs to undergo the maximum volume contraction, contributing to an increased interaction between the FA$^+$ in the cavities of Pb–I octahedral frameworks and causing the bodies of such octahedral frameworks to improve the stability of the entire FAPbI$_3$ SC.[34,35] Fig. 1c and S5 show the Fourier transform infrared (FTIR) spectra of FAPbI$_3$ SCs based on different orientations. In comparison with those based on (110) and (111) orientations, the most obvious redshift phenomenon of the C═N stretching vibration was observed at 1719.5 cm^{-1} for the (100) oriented SCs.[36,37] This suggests that the C═N bond energy is reduced due to stronger hydrogen bonding between FA$^+$ and the Pb–I octahedral framework.[38,39] Subsequently, scanning electron microscope (SEM) images were recorded to observe the prepared FAPbI$_3$ SCs with different facets. As shown in Fig. S6, the obtained (100) facet was entirely dense while holes and cracks formed on the obtained (110) and (111) facets. This characteristic contributes to the highest density exhibited by the GVL-based (100) oriented FAPbI$_3$ SCs (Fig. 1d), because of the minimal temperature dependence and the lowest crystallization temperature for the precursor dissolved in GVL (Fig. S7).[40,41]

To explore the mechanism of regulated orientations for FAPbI$_3$ SCs which are induced by the selected solvents, contact angle measurements were performed to explore the wettability of the precursor solutions with saturated concentrations in GVL, GBL and 2 ME solvents on the prepared (100), (110) and (111) facets of FAPbI$_3$ SCs (Fig. S8). The corresponding results were analyzed in Fig. 1e. After solvent replacement, the contact angles (θ) of the precursor solutions on these three crystal facets exhibit remarkably distinct trends. Notably, for the precursor solutions in GVL, GBL, and 2-ME, the maximum θ values (i.e., minimum surface energy) are observed on the (100), (110), and (111) facets, respectively.[42] According to the Gibbs–Curie–Wulff theorem, $\sum_i \sigma_i A_i$ is a minimum, where σ_i is the specific surface free energy per unit area of the crystal face (i) and A_i is the area. Thermodynamically, when a crystal achieves equilibrium with its surroundings, the total surface energy must reach a minimum state under constant volume conditions. Consequently, the morphology of crystal facets exhibits an inverse proportionality to their respective surface energies.[43–45] The trends in the surface energies of crystal facets across these three solvents are illustrated in Fig. 1f.[46–48] Notably, the crystal facets
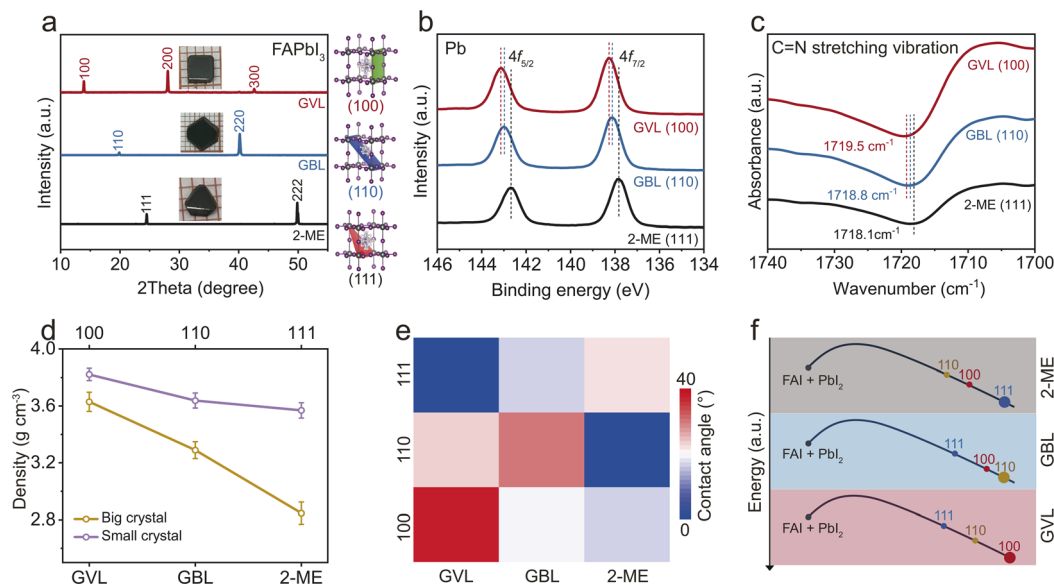
Fig. 1 (a) XRD patterns, (b) XPS spectra of Pb 4f, and (c) FTIR spectra measured on the three facets of FAPbI$_3$ SCs. (d) Density comparison of FAPbI$_3$ SCs grown with dominant (100), (110), and (111) orientations based on small size (~2 mm) and large size (~8 mm). (e) The contact angle trends of the precursor solutions with saturated concentrations in GVL, GBL and 2-ME solvents on the prepared (100), (110) and (111) facets of FAPbI$_3$ SCs. (f) The sketch map of the trend of facets' surface energies in different solvents.

exhibiting the lowest surface energy vary distinctly among these solvents. This phenomenon provides a robust theoretical basis for understanding why the (100), (110), and (111) facets for FAPbI$_3$ SCs preferentially form in the solvents of GVL, GBL, and 2 ME, respectively.

Optical-electrical properties

Theoretically, the (100) facet is electrically neutral with saturated bonds, whereas the (110) and (111) facets exhibit positive and negative electrical properties, respectively, both of which are associated with unsaturated bonds. Hence, the (100) orientation is more conducive to suppressing trap density and unnecessary ion migration compared to the (110) and (111) orientations.[22,24,30] Given that the performance of SC-based devices critically relies on the carrier behaviors, we utilized a series of characterizations to evaluate the optical-electrical properties of the SCs. Fig. 2a shows the photoluminescence (PL) mapping measurements of the samples. The increasingly redshifted trend of the average PL peak positions (Fig. S9) was observed for the SCs with (111), (110) and (100) facets, which corresponds to the results obtained from steady-state PL spectra (Fig. S10). This phenomenon is attributed to the release of stress in the crystals.[7,49] Additionally, the highest PL intensity occurring in the (100)-based SCs indicates this orientation has the best effect on inhibiting non-radiative recombination and decreasing the density of deep-level traps. This conclusion has been further verified by the TRPL spectra (Fig. 2b) and the transient reflectance (TR) measurements (Fig. S11), revealing that charge carriers excited on (100)-based SCs exhibit superior average lifetimes (Tables S1 and S2). Fig. 2c presents the results of electron and hole trap state densities (n_e and n_q) of the FAPbI$_3$ SCs with different crystal orientations, as calculated by the

space-charge-limited current (SCLC) measurements of electron-only and hole-only devices (Fig. S12). The (100)-based devices displayed the lowest n_e and nq values of the three samples, indicating the lowest non-radiative recombination of the (100) orientation benefited from the minimum trap state densities.

The ionic migration in organic–inorganic hybrid perovskites can severely degrade the stability and performance of their optoelectronic devices.[50,51] As depicted in Fig. 2d, significantly different hysteresis phenomena were observed from the forward and reverse scan I–V curves. Specifically, (110) and (111) -based samples presented more severe hysteresis than the (100) one, suggesting that few ionic migrations existed in (100) facets compared to (110) and (111) crystal orientations, due to the reduction of trap states. This result was further verified by the temperature-dependent conductivity characteristics (Fig. 2e and S13). The ion migration activation energy of the (100)-based sample was measured to be 0.304 eV, which is larger than the values of 0.251 eV and 0.179 eV measured for the samples based on (110) and (111). These findings demonstrate that ionic migration could be effectively suppressed through controlling the growth of the preferred orientation in FAPbI$_3$ SCs. Therefore, due to the low trap states and suppressed ion migration, the largest $\mu\tau$ product was detected for the (100)-based SCs (Fig. 2f), revealing that FAPbI$_3$ SCs with (100) crystal orientation has great potential to realize excellent performance in photodetectors.

Performance of photodetectors

Further, we fabricated planar photoconductive detectors with Au/crystal/Au structure (see the Experimental section for details) based on FAPbI$_3$ SCs with (100), (110) and (111) facets, respectively (Fig. 3a). These prepared devices were not assisted
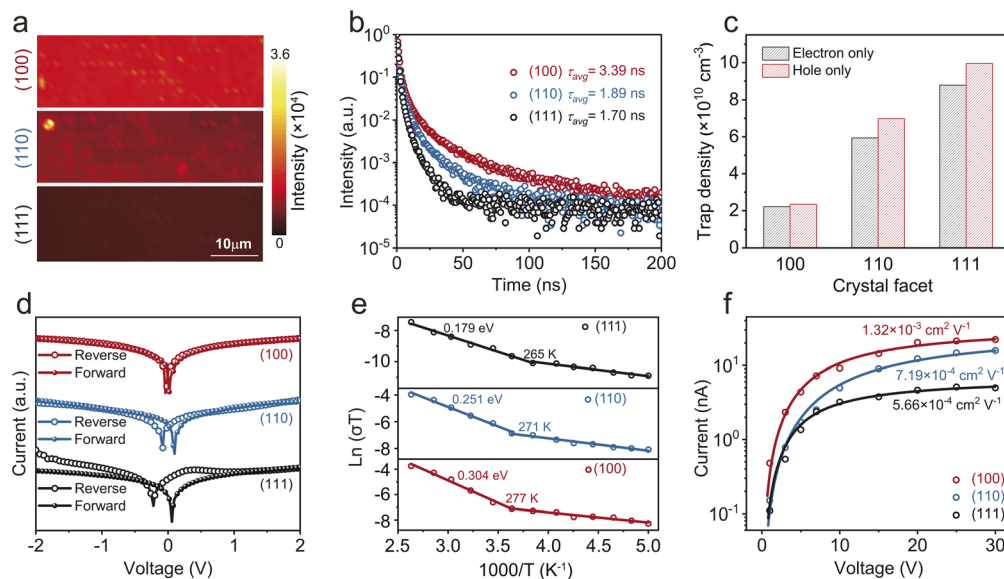
Fig. 2 (a) PL mapping, (b) TRPL spectra, (c) trap density of hole and electron devices, (d) dark current hysteresis measurements, (e) temperature-dependent conductivity measurements and (f) photoconductivity measurements on (100), (110), and (111) facets.

by any charge transport materials. The (100)-based one exhibited significantly lower dark current than the other two (Fig. 3b), suggesting fewer trap defects for the (100) facet can enhance the sensitivity of photodetectors, which is in accordance with the resistance results in Fig. S14.[52] Subsequently, sun illumination was applied to the three photodetectors (Fig. S15) where the intensity increased from 0.3 to 100 mW cm^{-2}. As shown in Fig. S16, at a bias voltage of 3 V, the photocurrent increases with illumination intensity, and the device with the (100) facet exhibits a higher response in comparison with those with (110) and (111) facets. These results are consistent with the switching

response of the photodetectors in Fig. 3c. The broader spectral response capability was further tested, and the (100)-based device showed higher values in both responsivity (R) (Fig. 3d) and detectivity (D^*) (Fig. S17) compared to the other two facet-based devices in the entire visible light spectrum. Specifically, Fig. 3d shows the photocurrent responsivity in the wavelength range from 300 nm to 800 nm. The strongest responsivity observed from the (100)-based device indicates (100)-based FAPbI$_3$ SCs possess the lowest density of deep-level defects. Based on these findings, we conducted systematic photo-response evaluation for the remarkable (100)-oriented devices
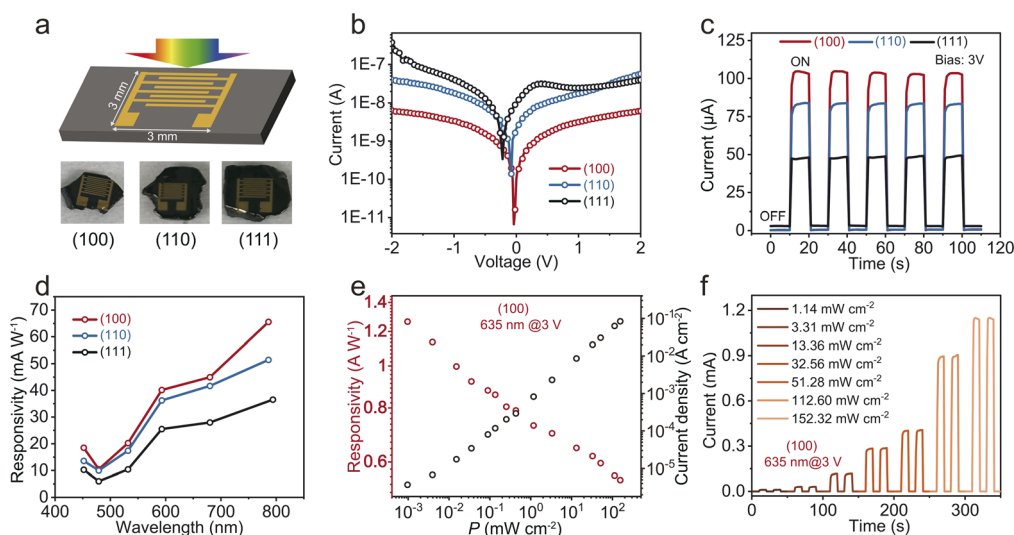

Fig. 3 (a) Schematic diagram and photograph of lateral structure photodetectors fabricated on (100), (110) and (111) facets. (b) Current–voltage (I–V) curves in the dark, (c) photocurrent time response under an ON/OFF interval of 10 s illumination with 1 SUN (100 mW cm^{-2}), (d) wavelength-dependent photo-response, (e) current density and responsivity of photodetectors against light power density, and (f) time dependent current curves for photodetectors under a series of light illumination intensities with 635 nm at a bias of 3 V.

under a 635 nm laser within a wider range of illumination intensities (Fig. S18). The decrease of responsivity with the enhancement of incident illuminated power stems from the photocurrent saturation phenomenon caused by the increased carrier recombination efficiency induced by high incident power (Fig. 3e).[53–56] Under an exceptionally low illumination of 8.6×10^{-4} W cm^{-2}, responsivity with a value of 1.26 A W^{-1} was obtained, as well as an EQE of 248.75% (Fig. S19a) and a detectivity (D^*) of 1.03×10^{13} Jones (Fig. S19b). Fig. 3f illustrates a sensitive switching response of the photodetector under different power densities. The ON/OFF ratio reached 8.84×10^4 at the highest power density of 0.152 A cm^{-2}, thanks to the low dark current and enhanced photocurrent which result from the low defect density.

Performance of X-ray detectors

We further assessed the X-ray detection performance of the same planar-structured FAPbI$_3$ SC devices with different facets (Fig. S20). The incident energy of X-rays is 30 keV. Compared to vertical devices, the electrode spacing can be designed to be very small for planar devices which tend to be more suitable under low X-ray dose (low detection limit) and low voltage operation.[57] I–V curves show X-ray response was suppressed when the X-ray dose was as low as 0.69 µGy$_{air}$ s^{-1} (Fig. S21). By tuning the X-ray source on and off, the response currents of the three SC detectors under different dose rates ranging from 21.4 to 0.69 µGy$_{air}$ s^{-1} were measured at 1 V bias (Fig. S22a). The (100) facet device achieves superior baseline stability compared to unstable baselines observed in the devices with (110) and (111) orientations (Fig. S22b). This enhanced stability stems from suppressed ionic migration as discussed above. As displayed in Fig. S22c, the response current density varied linearly with the

X-ray dose rate.[58] Notably, the (100) facet device exhibits superior sensitivity (6.3×10^4 µC Gy$_{air}$$^{-1}$ cm^{-2}), representing 2-fold and 74-fold enhancements over the (110)– and (111)-oriented counterparts, respectively. Comparison in Fig. S23 and Table S3 highlights that the (100) facet FAPbI$_3$ SC detector exhibited excellent performance in terms of sensitivity at a low electric field. To our knowledge, the obtained sensitivity is the highest value reported so far in all the perovskite photodetectors without charge transport layers when electric field is less than 10 V mm^{-1}. Such tested sensitivity is higher than the calculated maximum theoretical sensitivity (the calculated equation is presented in the SI), indicating that the photoconductive gain induced by shallow trap states functions in our devices under biased conditions.[4,5] This excellent performance demonstrates its significant potential for application in self-powered detection. Thus, we conducted the X-ray response measurement at a bias of 0 V (Fig. 4a). Strikingly, the (100) facet device presented an outstanding sensitivity of 4940 µC Gy$_{air}$$^{-1}$ cm^{-2} (Fig. 4b). This impressive sensitivity value is 247 times higher than that of the state-of-the-art commercial a-Se detectors (20 µC Gy$_{air}$$^{-1}$ cm^{-2})[1,14] and also shows an overwhelming advantage when compared with other reported self-powered perovskite X-ray detectors without the assistance of charge transport layers, including perovskite heterojunction detectors (Fig. 4c and Table S4). Such tested sensitivity is lower than the calculated maximum theoretical sensitivity, indicating the photoconductive gain induced by shallow trap states is not significant under self-powered conditions.[4,5] Additionally, benefiting from the high charge collection efficiency and low dark current, a very low detection limit of 41.1 nGy$_{air}$ s^{-1} was extracted from Fig. S24, which is almost two orders of magnitude lower than the requirement for regular medical diagnostics (5.5 µGy$_{air}$ s^{-1}).[1,2,59] The comparison with recently reported values is
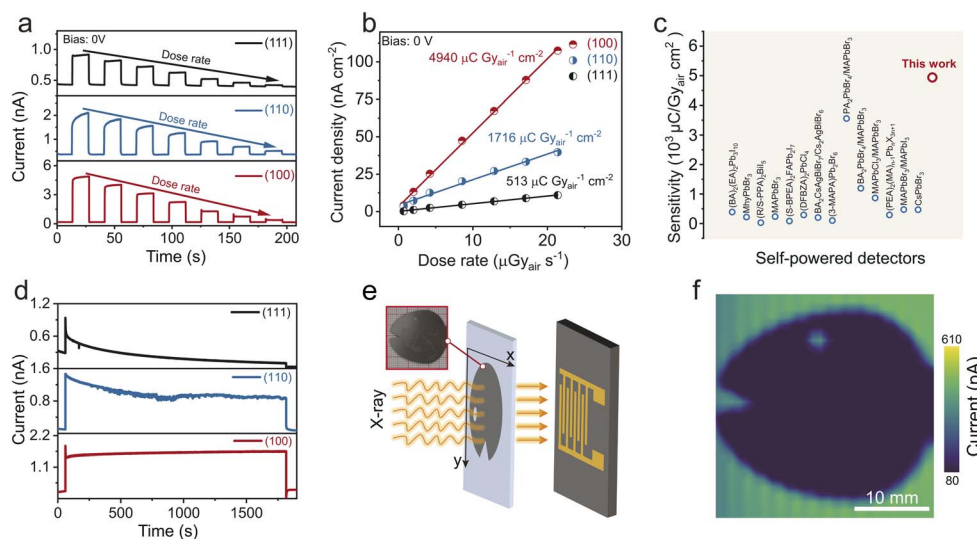
Fig. 4 (a) Switching X-ray responses to different dose rates (21.39−0.69 µGy$_{air}$ s^{-1}) and (b) current density as a function of the X-ray dose rate of the devices based on (100), (110) and (111) facet FAPbI$_3$ SCs at 0 V bias. (c) Comparison of X-ray sensitivity for (100) facet FAPbI$_3$ SC detectors in this work and previous literature. (d) Response currents under continuous X-ray irradiation of the (100), (110) and (111) facet FAPbI$_3$ SC detector under X-ray irradiation. (e) Schematic illustration of the X-ray imaging system applied in this work. Inset: a fish head used for X-ray imaging. (f) X-ray image of a fish head under 0 V bias at a dose rate of 4.2 µGy$_{air}$ s^{-1}.

summarized in Table S4, further highlighting the superior detection capability of our device.

For practical applications, the working stability of the detector is a key indicator to evaluate its usability in X-ray imaging. Fig. 4d presents the stability of response currents under continuous X-ray irradiation for (100), (110) and (111) oriented $FAPbI_3$ SC self-powered detectors in the air. In contrast to (110) and (111), the (100) device displayed a very stable baseline. Building on this, the (100) facet $FAPbI_3$ SC X-ray detector was applied to perform X-ray imaging at a dose rate of 4.2 μGy_{air} s^{-1} under 30 keV X-ray irradiation (Fig. 4e). The self-powered (100) facet device captured a clear X-ray image of the metal fish head as shown in Fig. 4f. Given that commercial X-ray detectors require a high electric field (*e.g.*, a-Se, 10 000 V mm^{-1}; CZT, 100–1000 V mm^{-1}), the exceptional self-powered capability of (100)-oriented $FAPbI_3$ single-crystal X-ray detectors demonstrates their potential as an ideal candidate for future medical diagnostic applications.

Conclusions

Herein, $FAPbI_3$ single crystals (SCs) with (100), (110) and (111) facets were synthesized by inducing the target facets to achieve the lowest surface energy facets in specific solvents. Among them, the (100) facet $FAPbI_3$ SCs grown in GVL exhibit superior crystalline quality with minimal defects, which effectively suppresses ionic migration and enhances charge collection efficiency. Benefiting from this, (100) facet $FAPbI_3$ SCs presented exceptional response performance under both visible-light and X-ray illuminations, outperforming their (110) and (111) counterparts. Remarkably, the planar (100) devices operate in a self-powered mode without transport layers, achieving a sensitivity close to 5000 μC Gy_{air}^{-1} cm^{-2}, which is 247 times higher than that of commercial a-Se detectors and represents the record value among all reported perovskite self-powered X-ray detectors without transport layers. Importantly, they also exhibit ultralow detection limits under low-energy irradiation and zero-bias operation, highlighting their potential for low-dose medical imaging. Nevertheless, challenges such as long-term stability, encapsulation, and large-area scalability still need to be addressed. Taken together, these findings not only underscore the promise of orientation engineering for advancing perovskite single-crystal detectors but also point toward future research directions for realizing practical, next-generation self-powered X-ray imaging technologies.

Experimental

Growth of $FAPbI_3$ SCs

$FAPbI_3$ SCs were grown with the method of inverse temperature crystallization according to previous publications.[23–25] Specifically, FAI and PbI_2 were mixed in a ratio of 1 : 1 (molar) in GVL and GBL at room temperature and the precursor concentrations were 0.33 M and 1.05 M, respectively. Then, the solutions were filtered into 20 mL glass vials using PTFE filters with a 0.8 μm pore size. The vials were placed in an oil bath at 60 °C and kept for 5 hours. After that, the GBL solutions were slowly heated

from 60 °C to 120 °C at a ramp rate of 5 °C per hour and $FAPbI_3$ started to appear in the bottom of the vials. For GVL solutions heated from 60 °C to 90 °C at a ramp rate of 5 °C per hour, the temperature was then increased from 90 °C to 93 °C at a slow rate of 0.2 °C per hour. Regarding 2 ME, FAI and PbI_2 were dissolved in a molar ratio of 1 : 0.85 while the precursor concentration was 0.6 M. After filtration, 2 ME solutions were slowly heated from room temperature to 80 °C at a rate of 5 °C per hour. After maintaining this temperature for 5 hours, 2 ME solutions were further heated from 80 °C to 95 °C at a slow rate of 0.2 °C per hour. All crystals grown from the three solvents were prepared under optimized conditions, thereby minimizing the influence of solvent purity, precursor concentration, and crystallization kinetics in this study.

Fabrication of $FAPbI_3$ SC detectors

The grown $FAPbI_3$ SC was polished to make its surface smooth. Planar-structured photoconductive detectors were fabricated by depositing 100 nm interdigital Au electrodes *via* thermal evaporation with a 100 μm bridging-gap electrode width. Afterward, copper wire was bonded to the two ends of the electrode by silver glue for electrical characterization of detectors.

Author contributions

Y. Z. and Y. W. designed and directed the research. F. L. performed all the experiments and analysed the data. Y. Z. participated in all the data analysis. P. W and H. W. contributed to X-ray detector measurements. J. G., Y. L. and H. W. contributed to single crystal characterization. W. Z. participated in photodetector measurements. Z. D., J. W. and Y. M. W contributed to contact angle data analysis. B. L., Y. M. and Y. C. were involved in the discussion of results and manuscript writing. F. L., Y. Z., Y. W. and Y. Z. drafted, revised, and finalized the manuscript.

Conflicts of interest

There are no conflicts to declare.

Data availability

The data supporting this article have been included as part of the supplementary information (SI). Supplementary information: materials, characterizations, methods, schematic diagram of the synthesis process, Tauc plots, lattice parameters, XPS spectra, FTIR, SEM, solubility curves, contact angle images, PL, TR , SCLC, additional *I–V* curves, photocurrent as a function of the light irradiance power density, detectivity as a function of the wavelength and light irradiance power density, EQE, photograph of X-ray detector testing equipment, switching X-ray responses, SNR as a function of the X-ray dose rate, and device performance comparison. See DOI: https://doi.org/10.1039/d5sc04089b.

Acknowledgements

References

1 H. Wei and J. Huang, *Nat. Commun.*, 2019, **10**, 1066.

2 S. You, Z. K. Zhu, S. Dai, J. Wu, Q. Guan, T. Zhu, P. Yu, C. Chen, Q. Chen and J. Luo, *Adv. Funct. Mater.*, 2023, **33**, 2303523.

3 Z. Li, F. Zhou, H. Yao, Z. Ci, Z. Yang and Z. Jin, *Mater. Today*, 2021, **48**, 155.

4 M. Girolami, F. Matteocci, S. Pettinato, V. Serpente, E. Bolli, B. Paci, A. Generosi, S. Salvatori, A. Di Carlo and D. M. Trucchi, *Nano Micro Lett.*, 2024, **16**, 182.

5 H. Tsai, F. Liu, S. Shrestha, K. Fernando, S. Tretiak, B. Scott, D. T. Vo, J. Strzalka and W. Nie, *Sci. Adv.*, 2020, **6**, eaay0815.

6 A. K. Jena, A. Kulkarni and T. Miyasaka, *Chem. Rev.*, 2019, **119**, 3036.

7 D. Chu, B. Jia, N. Liu, Y. Zhang, X. Li, J. Feng, J. Pi, Z. Yang, G. Zhao and Y. Liu, *Adv. Sci.*, 2023, **9**, eadh2255.

8 T. Yang, F. Li and R. Zheng, *Mater. Adv.*, 2021, **2**, 6744.

9 S.-T. Dong, Z. Fu, M. Yu, J.-L. Jiang, X. Jin, Y.-H. Guo, L. Wang and Y.-M. Zhang, *CrystEngComm*, 2022, **24**, 2100.

10 P. Calado, A. M. Telford, D. Bryant, X. Li, J. Nelson, B. C. O'Regan and P. R. Barnes, *Nat. Commun.*, 2016, **7**, 13831.

11 T. Kim, S. Park, V. Iyer, B. Shaheen, U. Choudhry, Q. Jiang, G. Eichman, R. Gnabasik, K. Kelley and B. Lawrie, *Nat. Commun.*, 2023, **14**, 1846.

12 K. Tao, C. Xiong, J. Lin, D. Ma, S. Lin, B. Wang and H. Li, *Adv. Electron. Mater.*, 2023, **9**, 2201222.

13 X. Zhang, T. Zhu, C. Ji, Y. Yao and J. Luo, *J. Am. Chem. Soc.*, 2021, **143**, 20802.

14 Q. Guan, S. You, Z. K. Zhu, R. Li, H. Ye, C. Zhang, H. Li, C. Ji, X. Liu and J. Luo, *Angew. Chem., Int. Ed.*, 2024, **63**, e202320180.

15 J. Wu, L. Wang, A. Feng, S. Yang, N. Li, X. Jiang, N. Liu, S. Xie, X. Guo and Y. Fang, *Adv. Funct. Mater.*, 2022, **32**, 2109149.

16 T. He, S. Li, Y. Jiang, C. Qin, M. Cui, L. Qiao, H. Xu, J. Yang, R. Long and H. Wang, *Nat. Commun.*, 2020, **11**, 1672.

17 Y. He, I. Hadar and M. G. Kanatzidis, *Nat. Photonics*, 2022, **16**, 14.

18 C. Ge, Y. Li, H. Song, Q. Xie, L. Zhang, X. Ma, J. Liu, X. Guo, Y. Yan and D. Liu, *Nat. Commun.*, 2024, **15**, 914.

19 Y. Liu, H. Ye, Y. Zhang, K. Zhao, Z. Yang, Y. Yuan, H. Wu, G. Zhao, Z. Yang and J. Tang, *Matter*, 2019, **1**, 465.

20 J. Ding, L. Jing, X. Cheng, Y. Zhao, S. Du, X. Zhan and H. Cui, *J. Phys. Chem. Lett.*, 2018, **9**, 216.

21 D. Kim, J.-H. Yun, M. Lyu, J. Kim, S. Lim, J. S. Yun, L. Wang and J. Seidel, *J. Phys. Chem. C*, 2019, **123**, 14144.

22 C. Ma, M. Grätzel and N.-G. Park, *ACS Energy Lett.*, 2022, **7**, 3120.

23 S. Dong, Z. Y. Hu, P. Wei, J. Han, Z. Wang, J. Liu, B. L. Su, D. Zhao and Y. Liu, *Adv. Mater.*, 2022, **34**, 2204342.

24 C. Ma, F. T. Eickemeyer, S.-H. Lee, D.-H. Kang, S. J. Kwon, M. Grätzel and N.-G. Park, *Science*, 2023, **379**, 173.

25 S. Li, Y. Xiao, R. Su, W. Xu, D. Luo, P. Huang, L. Dai, P. Chen, P. Caprioglio and K. A. Elmestekawy, *Nature*, 2024, **635**, 874.

26 X. Lin, H. Su, X. Shen, Z. Qin, M. Chen, Z. Zhang, G. Zheng, Y. Wang and L. Han, *Adv. Mater.*, 2025, **37**, 2418008.

27 P. Shi, Y. Ding, B. Ding, Q. Xing, T. Kodalle, C. M. Sutter-Fella, I. Yavuz, C. Yao, W. Fan and J. Xu, *Nature*, 2023, **620**, 323.

28 Q. Han, S. H. Bae, P. Sun, Y. T. Hsieh, Y. Yang, Y. S. Rim, H. Zhao, Q. Chen, W. Shi and G. Li, *Adv. Mater.*, 2016, **28**, 2253.

29 Y. An, J. Hidalgo, C. A. R. Perini, A.-F. Castro-Mendez, J. N. Vagott, K. Bairley, S. Wang, X. Li and J.-P. Correa-Baena, *ACS Energy Lett.*, 2021, **6**, 1942.

30 C. Ma, M.-C. Kang, S.-H. Lee, S. J. Kwon, H.-W. Cha, C.-W. Yang and N.-G. Park, *Joule*, 2022, **6**, 2626.

31 L. Chen, J. W. Yoo, M. Hu, S. U. Lee and S. I. Seok, *Angew. Chem.*, 2022, **134**, e202212700.

32 Y. Liu, J. Sun, Z. Yang, D. Yang, X. Ren, H. Xu, Z. Yang and S. Liu, *Adv. Opt. Mater.*, 2016, **4**, 1829.

33 Z. Li, S. Sun, H. Jiang, Z. Ding, C. Zhang, Z. Cui, Y. Wang, Y. Chen and H. Zhong, *Adv. Funct. Mater.*, 2024, **34**, 2407629.

34 D. Ghosh, A. R. Smith, A. B. Walker and M. S. Islam, *Chem. Mater.*, 2018, **30**, 5194.

35 W. Zuo, W. Fu, K. Wang, C. Das, M. M. Byranvand, K.-L. Wang, A. Chaudhary, J. Lim, M. Li and M. Saliba, *Energy Environ. Sci.*, 2024, **17**, 1407.

36 J. Zhang, X. Jiang, X. Liu, X. Guo and C. Li, *Adv. Funct. Mater.*, 2022, **32**, 2204642.

37 P. Wang, J. Guan, D. T. Galeschuk, Y. Yao, C. F. He, S. Jiang, S. Zhang, Y. Liu, M. Jin and C. Jin, *J. Phys. Chem. Lett.*, 2017, **8**, 2119.

38 J. Xiong, N. Eedugurala, Y. Qi, W. Liu, A. R. Benasco, Q. Zhang, S. E. Morgan, M. D. Blanton, J. D. Azoulay and Q. Dai, *Sol. Energy Mater. Sol. Cells*, 2021, **220**, 110862.

39 M. T. Weller, O. J. Weber, J. M. Frost and A. Walsh, *J. Phys. Chem. Lett.*, 2015, **6**, 3209.

40 A. Y. Alsalloum, B. Turedi, X. Zheng, S. Mitra, A. A. Zhumekenov, K. J. Lee, P. Maity, I. Gereige, A. AlSaggaf and I. S. Roqan, *ACS Energy Lett.*, 2020, **5**, 657.

41 L. Ma, Z. Yan, X. Zhou, Y. Pi, Y. Du, J. Huang, K. Wang, K. Wu, C. Zhuang and X. Han, *Nat. Commun.*, 2021, **12**, 2023.

42 J. Tam, B. Feng, Y. Ikuhara, H. Ohta and U. Erb, *J. Mater. Chem. A*, 2018, **6**, 18384.

43 A. W. Searcy, *J. Solid State Chem.*, 1983, **48**, 93.

44 A. Rohl and D. Gay, *J. Cryst. Growth*, 1996, **166**, 84.

45 R. Li, X. Zhang, H. Dong, Q. Li, Z. Shuai and W. Hu, *Adv. Mater.*, 2016, **28**, 1697.

46 S. Giljean, M. Bigerelle, K. Anselme and H. Haidara, *Appl. Surf. Sci.*, 2011, **257**, 9631.

47 M. Kalin and M. Polajnar, *Tribol. Int.*, 2013, **66**, 225.

48 M. Kalin and M. Polajnar, *Tribol. Lett.*, 2013, **52**, 185.

49 I. Borriello, G. Cantele and D. Ninno, *Phys. Rev. B: Condens. Matter Mater. Phys.*, 2008, **77**, 235214.

50 Y. Huang, L. Li, Z. Liu, H. Jiao, Y. He, X. Wang, R. Zhu, D. Wang, J. Sun and Q. Chen, *J. Mater. Chem. A*, 2017, **5**, 8537.

51 Y. Shao, Y. Fang, T. Li, Q. Wang, Q. Dong, Y. Deng, Y. Yuan, H. Wei, M. Wang and A. Gruverman, *Energy Environ. Sci.*, 2016, **9**, 1752.

52 Y. Zhao, X. Yin, P. Li, Z. Ren, Z. Gu, Y. Zhang and Y. Song, *Nano Micro Lett.*, 2023, **15**, 187.

53 P. Wang, H. Wang, J. Fu, H. Dong, W. Zhang, Z. Gao and Y. Shao, *ACS Photonics*, 2024, **11**, 5409.

54 C. K. Liu, Q. Tai, N. Wang, G. Tang, H. L. Loi and F. Yan, *Adv. Sci.*, 2019, **6**, 1900751.

55 Z. Chen, Z. Cheng, J. Wang, X. Wan, C. Shu, H. K. Tsang, H. P. Ho and J. B. Xu, *Adv. Opt. Mater.*, 2015, **3**, 1207.

56 J. M. Wu and W. E. Chang, *ACS Appl. Mater. Interfaces*, 2014, **6**, 14286.

57 X. Song, Q. Cui, Y. Liu, Z. Xu, H. Cohen, C. Ma, Y. Fan, Y. Zhang, H. Ye and Z. Peng, *Adv. Mater.*, 2020, **32**, 2003353.

58 L. Pan, S. Shrestha, N. Taylor, W. Nie and L. R. Cao, *Nat. Commun.*, 2021, **12**, 5258.

59 P. Jin, Y. Tang, D. Li, Y. Wang, P. Ran, C. Zhou, Y. Yuan, W. Zhu, T. Liu and K. Liang, *Nat. Commun.*, 2023, **14**, 626.